Superlattice formation in mixtures of hard-sphere colloids

Neil Hunt, Roger Jardine, and Paul Bartlett*
Department of Chemistry, University of Bath, Bath BA2 7AY, United Kingdom
(Received 4 February 2000)

We report a detailed experimental study of the superlattice structures formed in dense binary mixtures of hard-sphere colloids. The phase diagrams observed depend sensitively on the ratio $\alpha = R_S/R_L$ of the radii of the small (S) and large (L) components. Mixtures of size ratio $\alpha = 0.72$, 0.52, 0.42, and 0.39 are studied. The structures of the colloidal phases formed were identified using a combination of light-scattering techniques and confocal fluorescent microscopy. At $\alpha = 0.39$, ordered binary crystals are formed in suspensions containing an equal number of large and small spheres which microscopy shows have a three-dimensional structure similar to either NaCl or NiAs. At the larger size ratio, $\alpha = 0.52$, we observe LS_2 and LS_{13} superlattices, isostructural to the molecular compounds AlB_2 and $NaZn_{13}$, while at $\alpha = 0.72$ the two components are immiscible in the solid state and no superlattice structures are found. These experimental observations are compared with the predictions of Monte Carlo simulations and cell model theories.

PACS number(s): 82.70.Dd, 64.70.Dv, 64.75.+g

I. INTRODUCTION

Hard spheres constitute probably the simplest yet also one of the most important models of condensed-matter physics [1]. The phase behavior of hard spheres is determined by minimizing the free energy $F = U - TS$ or, since hard spheres are forbidden to interpenetrate and the internal energy U is a constant, by maximizing the entropy S. It was highly surprising, therefore, given the simplicity of the interactions in hard spheres, when experiments on colloidal particles [2] demonstrated that hard spheres of different sizes form equilibrium crystalline superlattices with large and highly complicated unit cells. Subsequent computer simulations [3] confirmed that a mixture with a radius ratio $\alpha = R_S/R_L$ of 0.58 formed two binary crystals, with stiochiometries LS_2 and LS_{13} (where L denotes the large particle). Clearly, given the subtlety of entropic effects at this size ratio, it is interesting to ask what structures might be stable at other size ratios. In general, the stability of a binary crystal, L_mS_n, depends on three variables, namely the size ratio α, the total packing fraction $\phi = \phi_L + \phi_S$, and the relative numbers of small and large spheres n_S/n_L. Clearly a determination of the phase behavior as a function of these three variables, α, ϕ, and n_S/n_L, represents a formidable task.

The present paper presents a first step in this direction where we report a comprehensive experimental study of the phase behavior of hard-sphere mixtures at size ratios $\alpha = 0.72$, 0.52, 0.42, and 0.39. Our motivation is threefold. First, while the stability of superlattice phases at size ratios *other* than $\alpha = 0.58$ has attracted considerable theoretical interest in recent years [4,5], there has been little experimental work that critically tests these theories. In the current paper we use a sterically stabilized colloidal system which other studies have demonstrated [6] provides a close experimental realization of classical hard spheres. Our experiments therefore model accurately a mixture of hard spheres. Second, the statistical properties of mescoscopic systems of particles are frequently dominated by entropic as opposed to enthalpic interactions. Consequently, the phase behavior of many colloidal systems can be appropriately mapped onto an effective hard-sphere system. Thus, for instance, LS_2 and LS_{13} structures have been observed in a range of mesoscopic systems including mixtures of charge-stabilized polystyrene spheres [7], two-dimensional arrays of gold clusters [8], and gem opals [9,10] in which the interactions are far from hard-sphere-like. Experiments on colloidal hard-sphere mixtures are important therefore as a simple reference case. Third, colloidal superlattices provide examples of three-dimensional photonic crystals with lattice parameters of the order of the wavelength of visible light and a range of different lattice symmetries. Such crystals could be used to create photonic band gaps (frequency ranges where light will not propagate because of multiple Bragg reflections) which are predicted to have unique and highly useful optical properties [11,12].

The paper is organized as follows. In Sec. II we summarize the current theoretical predictions for freezing in binary hard-sphere mixtures. The colloidal mixtures used are outlined in Sec. III and our detailed observations of the phase behavior are presented in Sec. IV. We then describe the scattering from a random-stacked LS superlattice in Sec. V and its microscopy in Sec. VI. Finally, we compare our results with theoretical predictions in Sec. VII and we collect our conclusions in Sec. VIII.

II. BINARY MIXTURES

At first sight the idea that entropy, which is normally taken to be a force-favoring disorder, should generate complex superlattice structures seems counterintuitive. It is frequently assumed, for instance, incorrectly, that complex interactions between particles are needed to generate complex phases. However, the physical origin of superlattice formation in hard-particle suspensions is both extremely simple and general [13]. The resolution of this paradox relies on distinguishing two components to the total entropy. The entropy of a system of spheres is composed of contributions

*Corresponding author.

associated with the degree of spatial ordering (the ''configurational'' entropy) and that associated with the space available to each particle for local motions (the ''free volume'' entropy). Confining the spheres of a binary suspension to the lattice cells of a superlattice structure decreases the configurational entropy compared with a disordered fluid phase. However, the particles within a superlattice have more local free volume in which to move than they do in the fluid, provided the superlattice fills space more efficiently than the fluid. Forming a superlattice increases the free volume entropy but at the expense of lowering the configurational entropy. At low concentrations, the configurational entropy dominates and the fluid is stable but with increasing concentration, the gain in free volume entropy on superlattice formation more than compensates for the loss of configurational entropy, and a stable superlattice is formed. These ideas have been confirmed by accurate calculations of the entropy from Monte Carlo simulations [3,4,14], density-functional theory [15], and cell-model calculations [5].

While the physical picture for superlattice formation is clear, there is as yet no theory which predicts *a priori*, given the size ratio, which structures are stable. All the current methods essentially go through a list of possible structures and analyze each in turn. The difficulty is the sheer number of potential candidates. The arguments given above do, however, suggest that one simple way to select feasible candidate structures is to use packing arguments. In particular, if a crystal structure has a high *close-packed* density (ϕ_{cp}), then, at the lower densities where freezing occurs, the constituent particles will have a large volume in which to move and a correspondingly higher free volume contribution to the entropy. On this basis, the entropy of each structure L_mS_n should mirror the maximum packing curve $\phi_{cp}(\alpha)$. Such space-filling arguments have been explored in detail by Sanders [9], who postulated that a superlattice will form only if its maximum packing fraction exceeds that for the pure one-component phase-separated crystals ($\phi_{cp}=\pi/\sqrt{18}\sim 0.74$).

The space-filling curves for a few selected binary structures are reproduced in Fig. 1, from which it is clear that over the range $0.3<\alpha<0.8$ only two structures, LS_2 and LS, fill space more efficiently than the fcc or hcp limit. The maximum packing principle accounts for the stability of the LS_2 crystal already seen in experiments at $\alpha=0.58$ and predicts furthermore that an LS compound, with a NaCl or a NiAs structure (both have identical values of ϕ_{cp}), should be stable around $\alpha=\sqrt{2}-1\sim 0.414$, for which the packing limit ($\phi_{max}=0.793$) is substantially above the uniform hard-sphere limit ($\phi_{cp}=0.7405$). A detailed study of Fig. 1 shows two further structures, the LS_{13} lattice ($\phi_{cp}=0.738$ at $\alpha=0.557$) and the CsCl structure ($\phi_{cp}=0.729$ at $\alpha=0.732$), which have packing limits close to, although slightly below, the monodisperse limit. While these structures should be unstable according to Sanders, their proximity to the fcc limit suggests they should be included in more detailed approaches.

Guided by maximum packing arguments, five different crystals have been suggested as possible equilibrium structures in mixtures of hard spheres.

(i) Substitutionally disordered fcc or hcp structure. In this crystal the large and small spheres are placed at random on a common fcc or hcp lattice. In the limit where the spheres have the same size, $\alpha\to 1$, we recover the single-component hard-sphere crystal. Computer simulations [16] predict that this structure is mechanically stable only if the sizes of the two particles are comparable, $\alpha>0.85$.

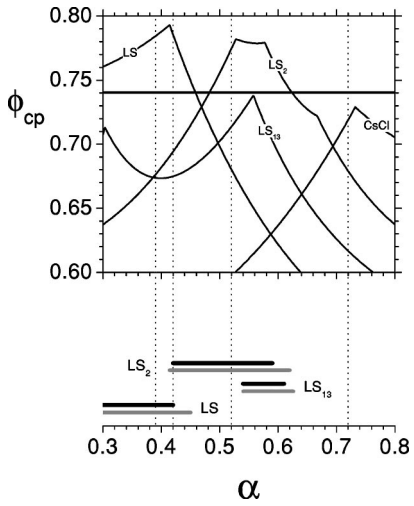

FIG. 1. The close-packing density (ϕ_{cp}) as a function of the size ratio α for the CsCl, LS_2, LS_{13}, and LS (NaCl or NiAs) structures. The packing limit of a fcc or hcp crystal of monodisperse spheres is shown by the horizontal line at $\phi_{cp}=0.7405$. The lower chart summarizes the regions of stability predicted by computer simulation (gray) [3,4,14] and cell calculations (black) [5,35]. The size ratios studied in the current work are shown dotted.

(ii) Ordered CsCl structure. This crystal consists of two interpenetrating simple-cubic lattices, one for each species. The structure has not been observed experimentally in colloidal hard-sphere mixtures, although it has been found in suspensions with a cross-attraction between large and small spheres [17]. Early density-functional calculations [18,19] predicted that CsCl should be stable in equimolar hard-sphere mixtures, but more recent and extensive simulation [14] and cell-model calculations [5] have not located a stable CsCl solid.

(iii) Ordered LS_2 structure. This crystal, which is isostructural with the alloy AlB_2, consists of a simple hexagonal crystal of large spheres with smaller particles filling all the trigonal cavities between the L layers. The structure has been observed [2] in mixtures of colloids with $\alpha=0.58$ and its stability confirmed by computer simulation [3].

(iv) Ordered LS_{13} structure. In the LS_{13} structure the large particles form a simple cubic lattice; each cubic subcell contains thirteen small particles, one at the body center and the remaining twelve on the vertices of an icosahedron surrounding the central particle. The icosahedra are rotated by 90° between adjacent subcells so that the full unit cell contains eight subcells and a total of 112 particles. The LS_{13} crystal has been seen in colloidal hard-sphere mixtures at $\alpha=0.58$ and 0.62 [2,20] and its stability was investigated by simulation [3].

(v) Ordered NaCl or NiAs structures (stiochiometry LS). The NaCl structure consists of a fcc lattice of large spheres with small spheres located on the octahedral interstitial sites, generating a second interpenetrating fcc lattice. The NiAs crystal is an analogous structure in which the large spheres are arranged in a hcp as opposed to a fcc lattice. The small

spheres still occupy octahedral sites but are now sited in a simple cubic rather than a fcc sublattice. Neither structure has been observed in experiments, although a stable NaCl crystal has been predicted by a number of theoretical studies [4,5,18,19].

The relative stability of these crystals depends on the density and composition of the mixture as well as the ratio of the sizes of the spheres. The most extensive analysis of the stability of hard-sphere mixtures has been performed using Monte Carlo simulation techniques [3,4,14,21,22] and a simple but reliable cell model developed by Cottin and Monson [5]. Density-functional theory has also been used to test the stability of different phases but only for *fixed* compositions. This restriction is not appropriate for our experiments so we shall not discuss these predictions further. Computer simulation and cell-model calculations, although based on very different approximations, reach essentially identical conclusions. For the size ratio range $0.3<\alpha<0.85$ these theories predict three stable superlattices: the LS_2 and LS_{13} lattices seen in experiments [2] at $\alpha=0.58$ and an *LS* compound with the NaCl (or NiAs [23]) structure. The range of size ratios over which each structure is stable is summarized at the bottom of Fig. 1. Very similar results were found using the cell model, although the widths of the stability domain predicted for LS_2 and LS_{13} are somewhat smaller [5]. Finally, both studies considered the stability of the CsCl lattice [5,14] but the crystal was predicted to be unstable with respect to phase separation into two pure solid phases.

The purpose of the present work is to compare these theoretical predictions with systematic experimental measurements on colloidal hard-sphere mixtures. The experimental system used in the current work is similar to the earlier work reported [2] at $\alpha=0.58$, but here we report data for a more extensive set of mixtures, extending the previous results to lower size ratios. In particular, we set out to address three questions. First, we study mixtures with size ratios $\alpha\sim0.4$ to clarify if the NaCl structure predicted is indeed observed experimentally. Second, we make measurements on systems with $\alpha=0.52$ with the aim of checking the theoretical prediction that this value of α marks the lower stability boundary of the LS_{13} superlattice. And finally, we explore the phase behavior at $\alpha=0.72$, close to the peak in the maximum packing curve for CsCl, where the formation of CsCl seems most likely.

III. EXPERIMENTAL DETAILS

The particles used in this study consisted of poly-(methyl methacrylate) (PMMA) spheres stabilized sterically by a thin ($\sim$10 nm thick) chemically grafted comblike layer of poly-(12-hydroxy stearic acid) (PHSA) chains. They were synthesized by a nonaqueous dispersion polymerization of a mixture of 98% methyl methacrylate (MMA) and 2% (by weight) methacrylic acid with a comb copolymer of PHSA and PMMA added as a stabilizer. Four different-sized particles (labeled $B-E$ in Table I) were prepared by changing the total monomer content following the methods described by Antl *et al.* [24]. Dye-labeled particles were made by repeating this synthesis using a mixture of methyl methacrylate (MMA), methacrylic acid, and 0.22 wt. % of the fluorescent monomer 2-(methyl-(8-nitro-benzo [1,2,5] oxadiazol-1-yl)-amino) methyl methacrylate (NBD-MMA) [25] as the constituent monomers. The resulting particles, labeled *A* in Table I, consisted of a fluorescent core and a nonfluorescent stabilizing layer of PHSA. The NBD-containing core absorbed at $\lambda=488$ nm and fluoresced intensely in a broadband of wavelengths centered around $\lambda\sim519$ nm. The particle radii and polydispersities [26] were determined from dynamic light-scattering measurements on dilute samples in *cis*-decahydronaphthalene (see Table I). Polydispersities of the nonfluorescent particles were of the order of 4%, while the fluorescent colloid *A* had a larger polydispersity of about 8%. Although polydispersities of this order affect the position of the freezing transition, the fact that all of our particles, including the fluorescent spheres, crystallize suggests that to a first approximation it is reasonable to neglect polydispersity.

TABLE I. Particles used in this work.

	Radius (nm)[a]			
Colloid	R (±3 nm)	R_{DLS} (±5 nm)	σ (±0.01)[b]	ϕ_m (±0.003)[c]
A[d]	175	175	$\sim$0.08	0.548
B	188	199	0.04	0.548
C	231	233	0.03	0.557
D	321	327	0.03	0.546
E	448	458	0.03	0.546

[a]Determined from crystallography and dynamic light scattering (DLS).

[b]Polydispersity $\sigma=\sqrt{\langle R^2\rangle}/\langle R\rangle$ determined by dynamic light scattering [26].

[c]Melting volume fraction. Computer simulation [27] gives $\phi_m=0.545$ for monodisperse hard spheres.

[d]Particle fluorescently labeled with NBD-MMA.

The particles were suspended in a near-refractive index-matching mixture of *cis*-decahydronapthalene (decalin, $n_{488}=1.4847$) and carbon disulphide (CS_2, $n_{488}=1.6483$). Carbon disulfide, in particular, has a substantial wavelength-dependent refractive index so, in practice, the particles and medium can be precisely matched only at one precise wavelength. We adjusted the proportions of the two solvents to minimize the scattering at $\lambda=568$ nm. With this choice, the change in refractive indices at the other laser wavelengths available to us, 488 and 647 nm, was sufficient to ensure that concentrated suspensions exhibited strong single scattering and little or no multiple scattering. Carbon disulfide is a good solvent for PMMA and swells the particles. However, the increase in size is small. Dynamic light-scattering measurements on dilute dispersions in pure CS_2 showed that equilibrium swelling is achieved within a few hours of contact with CS_2 and the resulting increase in the radius is $<2\%$. Index matching as well as making the scattering measurements feasible also suppresses the van der Waals forces. Indeed, previous studies have established that for suspensions of this type, the interparticle potential is steep, purely repulsive, and well approximated by a hard-sphere interaction. We confirmed that our particles behaved like hard spheres by observing the position of the fluid-crystal transition [6]. A series of one-component suspensions were prepared at concentrations which spanned the transition by centrifuging a stock solution and removing a known mass of solvent. The

samples were tumbled overnight to homogeneously mix the particles and solvent and were then left to stand undisturbed for observation. The heights of the fluid and crystalline phases were measured with a traveling microscope as a function of time. The linear dependence found for the height of each phase with time was extrapolated back to the start of the experiment to remove the effects of sedimentation and the equilibrium phase diagram determined. The melting point ϕ_m was found from linear regression through points in the coexistence region. Values for ϕ_m for each of the five colloids used are detailed in Table I. The close agreement seen between the experimental data and the value found from computer simulation [27] for the hard-sphere melting density, $\phi_m = 0.545$, confirms that the interparticle potential is close to hard sphere.

The structures of the crystals formed were studied using optical powder-diffraction techniques. Suspensions within the coexistence region were sealed inside optical quality 1 cm^2 rectangular glass cuvettes. The cuvette was placed at the center of an 150 mm diameter cylindrical bath filled with an index-matching mixture of 1, 2, 3, 4-tetrahydronapthalene (tetralin) and decalin. A parallel expanded beam from a krypton-argon laser ($\lambda = 647$ nm), approximately 15 mm in diameter, illuminated the sample through an optically flat window glued to the surface of the bath. The large scattering volume ensured that the intensity measured was a proper orientational average of the scattering from a powder of crystallites [28]. The index bath acted as a cylindrical lens, focusing scattered radiation onto a vertical slit which was placed in front of a photomultiplier tube. The collection optics were mounted on a computer-controlled turntable so that scattered intensities I could be measured over a range of angles from $\theta = 20°$ to 140° with a resolution of about 0.05°. With the laser beam perpendicular to the axis of rotation, the magnitude of the scattering vector, defined as $q = |k_i - k_s|$, is $q = (4\pi n/\lambda)\sin\theta/2$, where k_i and k_s are the incident and scattered wave vectors, n is the refractive index of the sample, and λ the laser wavelength.

The scattered intensity $I(q)$ measured from the pure one-component crystals showed the random-stacked close packed (rscp) powder pattern seen previously [28]. For samples in the coexistence region, the position q_{001} of the intense central peak [indexed to the (001) line in the reduced hexagonal basis of Sec. IV A] was used to obtain an accurate estimate of the effective hard-sphere radius from the identity $Rq_{001} = 3(\pi^2\phi_m/\sqrt{12})^{1/3} \sim 3.47$. The corresponding hard-sphere radii R are listed in Table I. The close agreement seen with the values obtained from dynamic light-scattering measurements (R_{DLS}) confirms the hard-sphere nature of these suspensions.

Binary suspensions were prepared by mixing stock solutions of the different-sized PMMA particles. Samples were concentrated by centrifugation. Four different particle combinations were studied (see Table II) with size ratios $\alpha = R_S/R_L$, calculated from the hard-sphere radii, of 0.39, 0.42, 0.52, and 0.72. At each α, samples were prepared at a number of volume fractions, $\phi = \phi_L + \phi_S$, which spanned the region between the monodisperse freezing $\phi_f = 0.494$ and glass transitions $\phi_g = 0.58$ where rapid crystallization is found for one-component suspensions [6]. Samples were prepared with a wide range of compositions, n_S/n_L, so as to cover the full extent of the fluid-solid transition in the $(\phi, n_S/n_L)$ plane. After preparation, each sample was homogenized by tumbling overnight and then inspected visually at regular intervals. While the samples were index-matched, they were not density-matched; the resulting sedimentation can dramatically affect the observed phase behavior in binary suspensions by altering the local density and composition within the sample. To prevent this gravity-induced separation, each sample was continuously rotated in a vertical plane at a rate of one revolution per day. Over one complete revolution, the effective sedimentation force averaged to zero and suspensions showed no signs of sedimentation [29]. The binary samples were sufficiently close to index-matched conditions that the first signs of crystallization were most easily detected by eye. The time required to first observe crystals from an initially homogenized suspension varied considerably but was on the order of weeks. As soon as crystallites could be seen, the structure and development of the sample were followed with regular powder-diffraction measurements. Samples were followed for up to a year from preparation.

TABLE II. Binary mixtures studied in this work. Size ratios determined by crystallography and dynamic light scattering (DLS).

	Radius ratio $\alpha = R_S/R_L$	
Colloid combination (S-L)	$\alpha \pm 0.01$	$\alpha_{\mathrm{DLS}} \pm 0.02$
$A-E$	0.39	0.36
$B-E$	0.42	0.43
$C-E$	0.52	0.51
$D-C$	0.72	0.71

The crystal structure in a couple of binary suspensions was also examined using confocal scanning laser microscopy (CSLM). Confocal images were collected on 100 μm thick, highly transparent PMMA suspensions with an index-matched solvent mixture of decalin and CS_2. The concentrated suspensions were stored in flat capillaries (2 mm wide, 5 cm long, 100 μm thick, with 170 μm thick walls) and sealed with araldite to prevent solvent evaporation. Although we made no quantitative measurements, binary suspensions crystallized noticeably faster in the thin capillary cells than the 1 cm path length optical cuvettes. Confocal micrographs of the colloidal crystals formed were obtained with an upright Leica TC NT microscope and the 488 nm line of an argon ion laser. We used a $100\times$ 1.3 NA oil immersion objective lens and a filter block which detected the fluorescence above 515 nm. Micrographs of 512 by 512 pixels were obtained in about 1 s by beam scanning.

IV. DETAILED OBSERVATIONS OF THE PHASE BEHAVIOR

The final phases observed in colloidal mixtures, with radius ratios of $\alpha = 0.72$, 0.52, 0.42, and 0.39, are summarized in Figs. 2(a)–2(d). The sequence of events after mixing depends sensitively on the radius ratio α and the relative numbers n_S/n_L or volume fractions ϕ_S/ϕ_L of small and large particles. Below, we describe our detailed observations.

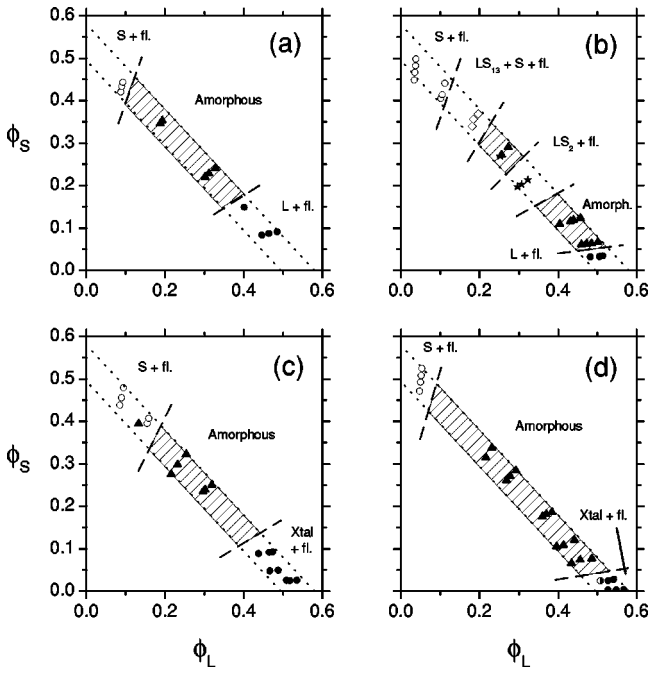

FIG. 2. Summary of final phase behavior observed for size ratios $\alpha=0.72$ (a), 0.52 (b), 0.42 (c), and 0.39 (d). The symbols denote the following: open circle, crystal of small spheres plus fluid; diamond, three-phase coexistence of LS_{13} crystal, crystal of large spheres, and fluid; triangle, glass; star, LS_2 crystal plus fluid; filled circle, crystal of large spheres plus fluid (for $\alpha=0.72$ and 0.52) or crystal (probably with defective NaCl structure—see text) plus fluid (for $\alpha=0.42$ and 0.39). The half-filled circle in (d) identifies the two-phase sample studied by confocal microscopy. The dashed lines correspond to the one-component hard-sphere freezing ($\phi_f=0.494$) and melting densities ($\phi_m=0.545$). All other lines are drawn in as guides to the eye.

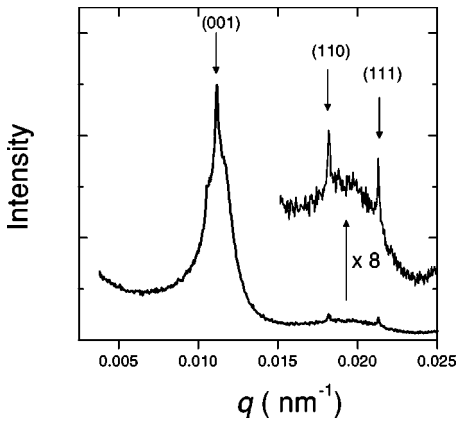

FIG. 3. Scattered light intensity from the coexisting crystalline phase formed in a binary mixture with size ratio $\alpha=0.72$, composition $n_S/n_L=0.5$ ($\phi_S/\phi_L=0.19$), and overall volume fraction $\phi_L+\phi_S=0.529$. The sharp Bragg peaks are indexed using the hexagonal rscp basis described in the text. The lattice constant (equal to the nearest-neighbor separation) is $a=671\pm6$ nm, which equates to a crystal density of $\phi_L=(8\pi/3\sqrt{2})(R_L/a)^3=0.65\pm0.02$.

A. Size ratio $\alpha=0.72$

Mixtures with a size ratio of $\alpha=0.72\pm0.01$ were prepared by combining large particles of colloid $D(R_L=321\pm3$ nm) with the smaller particles of colloid $C(R_S=232\pm3$ nm). A total of thirteen different mixtures was prepared, at five different number ratios, with total volume fractions in the range $0.507\leqslant\phi_L+\phi_S\leqslant0.576$. Three different classes of phase behavior were observed depending on the ratio of small to large spheres. Our observations are summarized in Fig. 2(a).

In samples with a large proportion of either the large or small species, colloidal fluid-crystal coexistence was observed. Small colloidal crystallites first appeared a few days after mixing. Nucleation appeared to be homogeneous with crystals appearing throughout the bulk of the sample. Over the next couple of weeks, these crystallites settled under gravity so that after 19 days a sharp interface was evident between an iridescent polycrystalline lower region and a slightly turbid colloidal fluid at the top. Light-scattering measurements, shown in Fig. 3, on the lower polycrystalline phase revealed a powder pattern profile similar to the distinctive patterns found previously in single-component hard-sphere suspensions [28].

The scattering from a pure hard-sphere system shows sharp Bragg peaks on top of a diffuse background. This distinctive powder pattern can be understood in terms of a random stacking of hexagonal close-packed planes of particles [28]. Starting with a single hexagonal close-packed plane (position *A*), there are two choices for the position of the next registered layer, *B* or *C*. Both of these possibilities lead to a close-packed structure. So, for instance, a fcc crystal can be built up from the stacking sequence *ABCABC*... or the symmetric twinned structure *ACBACB*..., while the sequence *ABABAB*... generates the corresponding three-dimensional hcp crystal. For the case of a purely random-stacked close-packed (rscp) sequence (*ABCBCA*...), the scattering is most conveniently described using a hexagonal layer of spheres as the basic structural unit.

The reciprocal space of a hexagonal layer with lattice constant a is a system of hexagonally arranged Bragg rods with a rod spacing in reciprocal space of $a^*=4\pi/a\sqrt{3}$ [30]. With a spacing between two close-packed layers of $c=a\sqrt{2/3}$, the unit vector in reciprocal space along the rods is of length $c^*=2\pi/c$ [31]. The intensity distribution along each of the Bragg rods with indices (h,k) depends on the stacking sequence of the hexagonal layers. When the layers are close-packed (consecutive layers occupy different lateral positions *A*, *B*, or *C*), the rods split into two distinct groups which are affected differently by randomness in the stacking sequence. For rods with $(h-k)=3n$, where n is an integer, the scattering intensity is always concentrated at the points (h, k, l), with l an integral, independent of the exact stacking order (provided it remains close-packed). On the other hand, if $(h-k)\neq3n$, the intensity distribution depends on the stacking sequence. For the twinned fcc structures, *ABCABC*... or *ACBACB*..., reciprocal-lattice points occur at $l=m\pm1/3$ with m an integral. For hcp, *ABABAB*... or *ACACAC*..., nodes occur at $l=m\pm1/2$. If stacking faults occur, the intensity maximum is broadened and spread along the rods. For randomly stacked layers, the intensity is continuously distributed along these rods with a maximum at $l=m\pm1/2$ and a minimum at $l=m$ with an intensity ratio of 9:1. The two sets of rods contribute in a qualitatively different manner to the observed powder-diffraction pattern. The high-intensity spots along the $(h-k)=3n$ rods, when orien-

tationally averaged, generate sharp Bragg peaks in the powder pattern. Conversely, the continuous intensity distribution along the $(h-k)=3n\pm1$ rods results in a broad, relatively featureless scattering peak in the powder spectrum. The rscp powder pattern of colloidal hard spheres consequently shows a distinctive combination of sharp Bragg peaks and broad diffuse regions of scattering.

Both of these features can be clearly identified in Fig. 3. Indeed, the close similarity between Fig. 3 and the results for the single-component hard-sphere crystals [28] suggests that the crystallites formed in this binary suspension are fractionated and consist of just one of the two species. The three sharp Bragg peaks visible in the powder pattern (Fig. 3) arise from scattering from the unbroadened (00) and (11) rods [and the equivalent rods $(2,\bar{1})$, $(1,\bar{2})$, $(\bar{1},\bar{1})$, $(\bar{2},1)$, and $(\bar{1},2)$]. Indexing these lines as the (001), (110), and (111) reflections gives a lattice parameter of $a=671\pm6$ nm. This is comparable to the diameter of the larger particle ($2R_L=642$ nm) so the crystal formed in this binary mixture must consist of a rscp crystal of large spheres.

A similar analysis of the scattering from all samples in the region $n_S/n_L\leqslant1.0$ or $\phi_S/\phi_L\leqslant0.4$ [represented by the filled circles in Fig. 2(a)] confirms fluid-crystal L coexistence. The crystals formed in the coexisting region of the phase diagram are strongly compressed in comparison with the melting density for one-component hard spheres of $\phi_m=0.545$. Measurements of the positions of the Bragg reflections revealed coexisting crystal densities as high as 0.65 in this region. Samples where there was an excess of small particles showed an analogous behavior. In the region $n_S/n_L\geqslant13(\phi_S/\phi_L\geqslant5)$, light crystallography confirmed the coexistence of a fluid and a crystalline phase, comprised of small spheres [indicated by the open circles in Fig. 2(a)]. Noticeably, however, the densities of the crystallites, as estimated from the positions of the Bragg peaks, were not as high as those found where large spheres were in excess with densities $\phi_S\sim0.54$, comparable to ϕ_m.

The most dramatic observation was in samples which contained sizable concentrations of both large and small species. Samples with compositions in the range $1.0<n_S/n_L<13.0$ $(0.4<\phi_S/\phi_L<5)$ remained single phase and homogeneous for at least six months. Light scattering revealed a ''fluidlike'' amorphous arrangements of particles.

B. Size ratio $\alpha=0.52$

Reducing the radius ratio to $\alpha=0.52\pm0.01$ significantly changed the observed pattern of behavior. Our findings are summarized in Fig. 2(b). Twenty-eight mixtures were prepared by combining large spheres ($R_L=448$ nm) of suspension E with small spheres of colloid $C(R_S=231$ nm) at eight different number ratios with volume fractions in the range $0.494\leqslant\phi_L+\phi_S\leqslant0.581$.

The most dramatic difference from the experiments at $\alpha=0.72$ is the formation of mixed binary or superlattice crystals. Superlattice colloidal crystals were found in mixtures with composition $n_S/n_L=14$ $(\phi_S/\phi_L=2)$. The superlattice phase appeared in coexistence with a second crystalline phase of pure small crystals and a fluid phase [the open diamonds in Fig. 2(b)]. Formation was exceedingly slow. A few days after mixing, iridescent specks of nucleating crystallites appeared throughout the samples and sedimented to form a polycrystalline layer. Light-scattering measurements revealed [Fig. 4(a)] that this crystalline layer consisted of a random close-packed crystal of small spheres. Only after four months did features first appear in the scattering profile characteristic of a superlattice structure [see Fig. 4(b)]. The intensity of the superlattice peaks grew rapidly over the next four weeks and then remained essentially unchanged for three months of observation. The regular positions of the sharp Bragg reflections evident in Fig. 4(d) are consistent with the formation of a cubic structure. Fitting the peak positions to $q_{hkl}=(2\pi/a)\sqrt{h^2+k^2+l^2}$ gives a cubic lattice constant a of 2460 ± 6 nm. The large lattice constant and the similarity of the scattering seen in Fig. 4(d) to previous measurements made on mixtures of $\alpha=0.58$ suggest that the structure formed is the cubic LS_{13} phase. Assuming an LS_{13} structure, the experimentally determined lattice constant gives a crystal density of $\phi_L+\phi_S=0.56$, which compares favorably with the overall density of the suspension $\phi=0.521$.

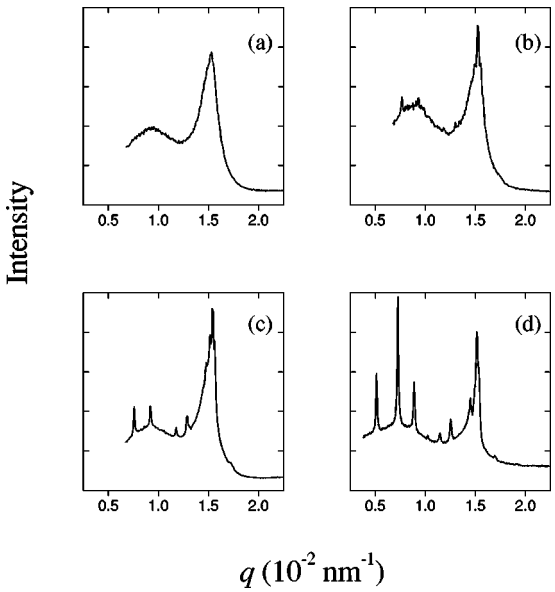

FIG. 4. The scattering from the bottom iridescent layer formed in mixture with $\alpha=0.52$, $n_S/n_L=14$ $(\phi_S/\phi_L=2)$, and $\phi=0.521$ measured (a) 107, (b) 116, (c) 130, and (d) 198 days after mixing. Pattern (a) shows that the first-formed crystalline phase consists of small (diffraction-broadened) crystallites of small spheres ($a=506$ nm, $\phi_S=0.56$). After ~110 days the low-q reflections of the LS_{13} superlattice become visible. The proportion of LS_{13} in the crystalline phase increases with time. The Bragg peaks in (d) are, in order of increasing q, the (200), (220), (222), (400), (420), (422), and (440) reflections of the LS_{13} structure, which gives a cubic lattice constant of $a=2460$ nm and a crystal density of $\phi=32\pi(R_L^3+13R_S^3)/(3a^3)=0.56$.

A second superlattice phase appeared in mixtures [marked by stars in Fig. 2(b)] with composition $n_S/n_L=5$ and 8 $(\phi_S/\phi_L=0.7$ and 1.1). The rate of crystallization was again slow with full crystallization taking about 80 days for $n_S/n_L=5$ $(\phi_S/\phi_L=0.7)$ and over 200 days for mixtures with $n_S/n_L=8$ $(\phi_S/\phi_L=1.1)$. Crystals were observed visually first in a narrow layer at the center of the sample cuvette. Analysis by powder light crystallography showed three relatively weak but sharp Bragg peaks superimposed on a broad

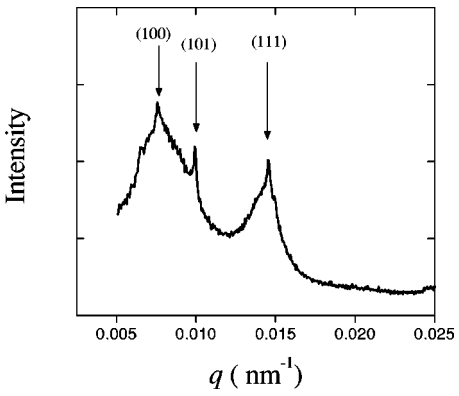

FIG. 5. The scattering from the bottom iridescent layer formed in a mixture of size ratio $\alpha=0.52$, composition $n_S/n_L=5(\phi_S/\phi_L=0.7)$, and volume fraction $\phi=0.509$. The Bragg reflections index on the hexagonal unit cell of the LS_2 superlattice. The featureless background scattering present indicates that the lower phase also probably contains amorphous material.

diffuse background (Fig. 5). The reflections measured from four different mixtures indexed on a hexagonal lattice, $q_{hkl}^2/4\pi^2=(4/3a^2)(h^2+k^2+hk)+(l^2/c^2)$, with a mean hexagonal interlayer spacing of $c/a=1.041\pm0.001$ and a mean lattice parameter of $a=950\pm2$ nm. The most plausible structure for the observed phase is the LS_2 lattice. Strong evidence for the formation of this structure in mixtures with $\alpha=0.52$ comes from a comparison with earlier data. The experimental c/a ratio differs by less than 0.4% from that found previously [2] and the crystal density, $\phi=0.622\pm0.004$, is similar to the values quoted in Ref. [14].

The two regions of superlattice formation were separated by a central band of compositions where samples remained amorphous ($n_S/n_L=8$ or $\phi_S/\phi_L=1.1$). In this region, crystallization was totally suppressed and mixtures remained amorphous during the year-long duration of our observations. Similar behavior was also observed in the second region of amorphous behavior for compositions $0.5<n_S/n_L<4$ $(0.07<\phi_S/\phi_L<0.6)$. Finally, close to the two axes the phase behavior is similar to that observed in the $\alpha=0.72$ system. So, for instance, two-phase coexistence of random-packed L crystals and fluid is found for $n_S/n_L\leqslant0.5$ $(\phi_S/\phi_L=0.07)$, while for $n_S/n_L\geqslant30$ $(\phi_S/\phi_L\geqslant4)$ the stable phase are crystals of small spheres and fluid.

It is instructive to compare the current observations for $\alpha=0.52$ with the experimental results obtained previously [14] for $\alpha=0.58$ and 0.62 (Fig. 6). It is clear that there are striking differences between these closely spaced sets of mixtures. First, the superlattice regions in the $\alpha=0.52$ phase diagram are narrow in extent in comparison with the well developed region of superlattice formation found for the $\alpha=0.58$ mixture. Second, there is a marked slowing-down in the rate of nucleation and growth of the LS_2 and LS_{13} phases as α is reduced towards 0.52. In the $\alpha=0.58$ mixture, crystallites of LS_{13} appeared within three days, with LS_2 formation taking about five weeks. In comparison, at $\alpha=0.52$, growth of LS_2 and LS_{13} required over three months. Finally, the phase diagram at $\alpha=0.52$ is more complicated than either the $\alpha=0.58$ or 0.62 diagrams. In particular, the two regions of superlattice coexistence are separated in the $\alpha=0.52$ system by an intervening amorphous region not

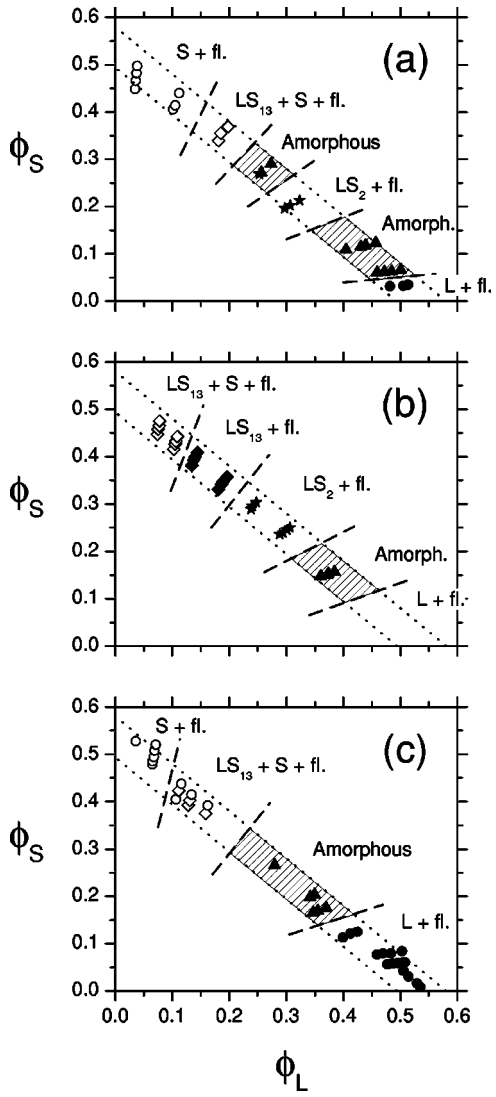

FIG. 6. A comparison of the experimental phase behavior seen in mixtures of size ratio (a) $\alpha=0.52$, (b) 0.58 and, (c) 0.62. The meaning of the symbols is the same as in Fig. 2. The regions of amorphous phases are shown shaded. The dashed lines correspond to the one-component hard-sphere freezing ($\phi_f=0.494$) and melting densities ($\phi_m=0.545$). All other lines are drawn as guides to the eye.

present for $\alpha=0.58$. These changes suggest that the LS_2 and LS_{13} phases are becoming increasingly less stable as the size ratio α is reduced.

C. Size ratio $\alpha=0.42$

Binary mixtures with radius ratios of $\alpha=0.42$ showed substantially different behavior from the $\alpha=0.52$ mixtures studied above. The most striking difference was observed in mixtures with sizeable number densities of each species. In the $\alpha=0.52$ system, these central compositions form superlattice phases. Reducing the radius ratio to $\alpha=0.42$ seemed to destabilize all crystalline phases. Those compositions which crystallized in the $\alpha=0.52$ system now remained totally amorphous. Our findings are summarized in Fig. 2(c). Twenty-one mixtures of radius ratio $\alpha=0.42\pm0.01$, at five different number ratios, were made by combining large colloidal particles from batch $E(R_L=448\,\text{nm})$ with smaller par-

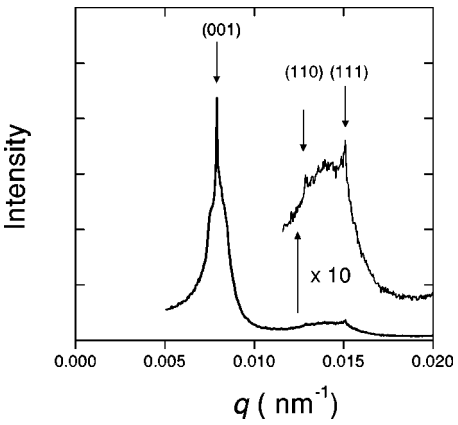

FIG. 7. Scattering from the crystalline layer formed in a suspension of ratio $\alpha=0.42$, $n_S/n_L=1(\phi_S/\phi_L=0.07)$, and $\phi=0.537$. The Bragg peaks are indexed on the rscp basis.

ticles from batch $B(R_S=188\,\text{nm})$ to give volume fractions in the range $0.525\leqslant\phi_L+\phi_S\leqslant0.565$. In a one-component system, suspensions with volume fractions in this range crystallize rapidly.

The sequence of behavior observed resembles, at least superficially, that reported above for the $\alpha=0.72$ system. So, for instance, in samples with an excess, by volume, of large spheres ($n_S/n_L=0.5$, 1, or 2), the final equilibrium state corresponded to a fluid-crystal coexistence. However, in comparison with the $\alpha=0.72$ system, crystallization was noticeably slower. For instance, $\alpha=0.72$ mixtures with $n_S/n_L=0.5$ formed small crystallites, just visible by eye (estimated size 10–15 μm), within two days of mixing. In the $\alpha=0.42$ system, mixtures with the same composition and total density took approximately 20 days for crystals to be observable. Over a couple of days, these small crystallites sank to the bottom of the sample cell and formed an iridescent crystalline layer. Figure 7 shows the powder-diffraction profile measured from the crystalline layer formed in a suspension with an equal number of large and small spheres and a total density of $\phi=0.537$. As is clear from a comparison between Fig. 7 and Fig. 3, the measured scattering profile resembles closely the scattering seen from a rscp crystal of large spheres.

While the evident similarities between the scattering observed in this region and that from a rscp crystal of large spheres seem, at first sight, to suggest that the crystalline phase is composed of a phase-separated crystal of large spheres, a closer study of the scattering data shows it to be inconclusive. The theoretical calculations outlined in Sec. II suggest that for $\alpha=0.42$ any one of a family of close-packed superlattice phases which includes NaCl and NiAs could be stable. Below we demonstrate that while the scattering from each of these structures is in principle different from each other and from the fractionated large-sphere crystal phases, under the conditions of our experiments the differences are small. To distinguish between the different superlattice structures and a rscp crystal of large spheres requires careful intensity measurements. Because of the high sensitivity of the particle scattering near index-match, these experiments are very demanding. Consequently, from scattering alone, we cannot identify the nature of the crystal seen in Fig. 7. We shall return to this point in Sec. VI.

Increasing the proportion of small spheres further reduced the rate of crystallization. In suspensions with $n_S/n_L=8$ ($\phi_S/\phi_L=0.6$), crystals were observed but only in the lowest volume fraction sample ($\phi=0.532$). Even in this sample the crystallites were sufficiently small that efforts to measure the scattering from the small proportion of crystalline material present were unsuccessful. With larger proportions of small spheres, $n_S/n_L=13$ or 25 ($\phi_S/\phi_L=1$ or 2), crystallization was totally suppressed and remained totally amorphous during our observations. Very large proportions of small spheres ($n_S/n_L=52,\phi_S/\phi_L=4$) gave mixtures which, once again, displayed two-phase coexistence. In these samples, flecks of colloidal crystallites appeared throughout the sample within about 30 days of mixing. The crystallites rapidly sedimented into an iridescent layer at the bottom of the cuvette. Powder-diffraction measurements gave results which were almost identical to the scattering from crystals of the small spheres alone. In this case there is no possibility of confusion between a crystal of small spheres and a NaCl-type superlattice, so we can confidently identify the crystalline phase formed in the mixture as a random-stacked crystal of small spheres.

D. Size ratio $\alpha=0.39$

To clarify, if the NaCl-type superlattice is formed at $\alpha\sim0.4$, the experiments detailed in Sec. IV C were repeated but with a mixture of fluorescent and nonfluorescent particles. The real-space structure of the crystals formed was studied using fluorescent confocal scanning laser microscopy (CSLM) and is discussed below in Sec. VI. Here we summarize the observed phase behavior.

Twenty-four binary mixtures were prepared by combining small fluorescent particles from batch A ($R_S=175\,\text{nm}$) with larger, nonfluorescent spheres of colloid $E(R_L=448\,\text{nm})$ to give a size ratio of $\alpha=0.39\pm0.01$. The mixtures studied are detailed in Fig. 2(d) together with a summary of the phase behavior found. The small particles were fluorescently labeled by incorporating the monomer 2-(methyl-(8-nitrobenzo [1,2,5] oxadiazol-1-yl)-amino) methyl methacrylate (NBD-MMA) into the core of the colloidal particle. The dye is absent from the surface of the particle so the interaction potential and the phase behavior of the small spheres ought not to be affected by labeling. Experiments confirm this prediction with suspensions of pure fluorescently labeled particles crystallizing rapidly with a melting density of $\phi_m=0.548$, which is close to the value expected for hard spheres ($\phi_m=0.545$). Furthermore, measurements of the scattered light intensity from the crystals, at long wavelengths ($\lambda=647\,\text{nm}$) where the particles do not fluoresce, reveal that the crystal has the rscp structure expected for colloidal hard spheres. Consequently, the differences observed between the phase diagrams of the fluorescent $\alpha=0.39$ and nonfluorescent $\alpha=0.42$ mixtures may be attributed to a change in the size ratio α and not to labeling.

Comparison of the two phase diagrams shows that reducing α from 0.42 to 0.39 broadens the extent of the amorphous region. So while for $\alpha=0.42$ the amorphous region extended over compositions from $8<n_S/n_L<25$ ($0.6<\phi_S/\phi_L<1.9$), the range has expanded to $2<n_S/n_L<50$ ($0.1<\phi_S/\phi_L<3.0$) by $\alpha=0.39$. In the $\alpha=0.39$ mixture, the

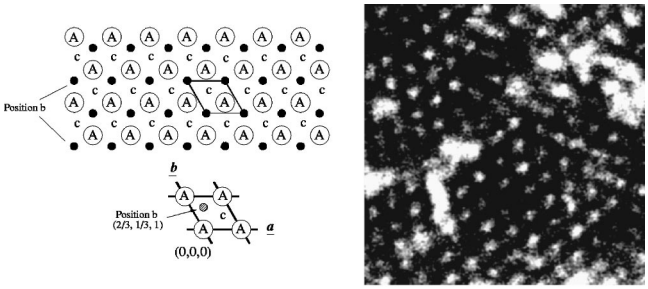

FIG. 8. (a) The (001) face of the NaCl crystal. The positions of the large spheres are labeled ''*A*.'' The small spheres (shown in bold) occupy the ''*b*'' set of interstitial sites while the ''*c*'' sites are vacant. The unit cell of the hexagonal layer is shown in bold. (b) CSLM image of ordered binary crystal formed in a suspension of size ratio $\alpha=0.39$, composition $n_L/n_S=1$ ($\phi_S/\phi_L=0.06$), and volume fraction $\phi=0.532$. The picture was taken with a 100 $\times$1.3 NA oil immersion lens and is 12.5 μm square. The hexagonal order of the small fluorescent particles is clearly visible.

two regions of fluid-crystal coexistence are extremely narrow and crystallization is essentially limited to mixtures very rich in either large or small spheres. Outside these compositions, mixtures remained amorphous on the time scale of the experiments. Finally, we note that samples containing an equal number of big and small spheres, $n_S/n_L=1$ ($\phi_S/\phi_L=0.06$), show fluid-crystal coexistence.

V. SCATTERING FROM *LS* SUPERLATTICES

The *LS* family of superlattices (NaCl, NiAs, and random-stacked analogs) consists of a close-packed layer of large spheres with small spheres occupying all the available octahedral interstitial sites in the resulting lattice. To understand why the scattered intensity is insensitive to the differences between these structures, it is advantageous to start from the basic element common to each of these structures—a single hexagonal slice containing both large and small particles. Each of the *LS* crystals is generated by stacking these slices in a different order. Figure 8(a) shows one such composite slice together with the conventionally defined hexagonal basis vectors **a** and **b**. The axis *c* is chosen as equal to the distance between two neighboring large-sphere layers and is set so that the layer of large spheres lies in the reference plane $c=0$. The slice consists of a hexagonal layer of large spheres with a further layer of small spheres situated in the plane $c=1/2$. The small spheres are positioned above the center of the equilateral triangle formed by the centers of the three adjoining large spheres in the $c=0$ reference plane. There are two ways in which the layer of small spheres may be placed on the reference layer *A* of large spheres, which are designated by *b* and *c* in Fig. 8(a). The position of the *b* sphere [shown in black in Fig. 8(a)] with respect to the large spheres in layer *A* is given by the vector $2\mathbf{a}/3+\mathbf{b}/3+\mathbf{c}/2$, while the *c* sphere is located at $\mathbf{a}/3+2\mathbf{b}/3+\mathbf{c}/2$. The full three-dimensional structure is obtained by stacking slices repeatedly on top of the slice shown in Fig. 8(a). The projection of each large-sphere layer on the reference plane ($c=0$) can take only one of three different positions—*A*, *B*, or *C*—if the structure is to be close-packed. In position *B* (or *C*), the large sphere in the second slice is placed above a vacant interstitial *b* (or *c*) site in the first slice.

The two simplest arrangements which are periodic are the NiAs lattice, consisting of a close-packed hexagonal stacking of large spheres (upper case) with small spheres (lower case) organized in vertical columns, *AcBcAcBcAcBc*, and the NaCl lattice where the arrangement of the large-sphere layers is fcc and the layers of small spheres generate a second interlocking fcc lattice, *AcBaCbAcBaCbAc*. One-component colloidal crystals are nearly always randomly stacked (with stacking sequences such as *ABCBCAB*... or *ACBABC*... rather than pure fcc or hcp) so similarly we expect that random superlattice structures such as *AcBaCaBaCbAcB* may occur. Here we show that the scattering from any of these structures closely resembles that of the identically stacked large-sphere crystal. To that end we shall consider in detail just one of the possible superlattice structures—namely the NaCl lattice. This is the most straightforward case to analyze but our arguments are readily extended to treat the other structures.

It is clear that for the NaCl structure *AcBaCb*... or its twin *AbCaBc*..., the periodicity and symmetry of the small-sphere lattice are the same as that of the large-sphere lattice (although displaced by $\Delta c=1/2$). This is very different from the behavior observed when either LS_{13} or LS_2 form, where the superlattice structures have a new symmetry and periodicity that is not shared with the one-component crystal. The origin of this difference lies in the nature of the NaCl structure, where the small spheres occupy interstitial sites rather than substitutional sites as in LS_2 or LS_{13}. Occupying interstitial sites does not alter the three-dimensional arrangement of the larger spheres so that the Bragg reflection conditions for the NaCl structure are identical to those for a fcc lattice of large spheres. Although the formation of NaCl does not alter the number of Bragg reflections, it does modify their intensity. In NaCl, the small-sphere lattice is displaced relative to the large-sphere lattice so that scattering from the small spheres is out-of-phase compared with the large-sphere scattering and the diffracted intensity is modulated.

The scattered intensity produced by a phase of partially disordered layers has been addressed by a number of authors. Excellent reviews are available in the textbooks on x-ray diffraction by Guinier [30] and Warren [32]. In the systems of interest to us, the three-dimensional (3D) close-packed structures are built up from 2D hexagonal slices and the intensity scattered by the crystal is concentrated along hexagonally arranged rods in reciprocal space (see Sec. IV A). The intensity along each of the (*h*,*k*) rods is determined by the stacking sequence of the layers. A general expression for this intensity $I_{hk}(l)$, for a system of *N* identical slices stacked along the *c* axis, has been derived by Guinier [30],

$$I_{hk}(l)=\frac{|F|^2}{N}\sum_{m=-N}^{m=N}\left(1-\frac{|m|}{N}\right)y_m\exp(2\pi ilm), \qquad (1)$$

where *l* is the distance along the rod expressed in units of $c^*=2\pi/c$ and *F* is defined by

$$F=\sum_p b_p e^{-2\pi i(hx_p+ky_p+lz_p)}, \qquad (2)$$

with b_p the amplitude scattered by each of the p particles contained within the unit cell. The function F is called, rather confusingly, the structure factor in the crystallography literature, although $|F|^2$ is actually the intensity scattered by a single unit cell and so is best thought of as a cell form factor. The function y_m summarizes the degree of correlation between layers. In detail, $|F|^2 y_m$ is the ensemble average $\langle F_n F^*_{n+m}\rangle$ of the product of the amplitudes scattered by two unit cells separated by a vertical distance mc along the c axis.

For the NaCl structure, *AcBaCb*..., we select the reference slice as $\overline{Ac}$ with a unit cell which contains a large sphere at position A and a second (small) sphere on the interstitial site c. The corresponding cell form factor, $|F_{Ac}|^2$, is readily calculated from Eq. (2) and the geometry of Fig. 8(a) as

$$|F_{Ac}|^2 = b_L^2 \cos^2 \pi\left(\frac{h-k}{3}+l\right) - 2b_L b_S \cos 2\pi\left(\frac{h-k}{3}-l/2\right)+b_S^2, \tag{3}$$

where b_L and b_S are the amplitudes of scattering from the large and small particles, respectively. The position of the $\overline{Ba}$ slice is translated by the vector $(2\mathbf{a}/3)+(\mathbf{b}/3)$ relative to the $\overline{Ac}$ slice so that the structure factor for a unit cell of slice $\overline{Ba}$ is

$$F_{Ba} = F_{Ac} e^{2\pi i[(h-k)/3]}. \tag{4}$$

Similarly,

$$F_{Cb} = F_{Ac} e^{-2\pi i[(h-k)/3]} \tag{5}$$

for the slice $\overline{Cb}$. Assuming fault-free fcc stacking, the autocorrelation function y_m may be calculated analytically from Eqs. (4) and (5) with the result $y_m = e^{-2\pi i m(h-k)/3}$. The intensity along the (h,k) row is then obtained from Eq. (1) as

$$I_{hk}(l) = \frac{|F_{Ac}|^2}{N}\sum_{m=-N}^{m=N}\left(1-\frac{|m|}{N}\right) y_m \exp(2\pi i m\Lambda) = |F_{Ac}|^2 \frac{\sin^2 \pi N\Lambda}{\sin^2 \pi\Lambda}, \tag{6}$$

where $\Lambda = l-(h-k)/3$. The intensity I_{hk} is a sharply peaked function whose maximum value is $|F_{Ac}|^2$, for integral values of Λ. As the number of layers increases, $N\to\infty$, it becomes a δ function. In general, there are two types of Bragg rods. For rods with $(h-k)=3n$, where n is an integer, there is a succession of nodes at integral values of l. On the other hand, for rods with $(h-k)=3n\pm 1$, the reciprocal-lattice points occur for $l=n\pm 1/3$. All intensity nodes have the same maximum value of $|F_{Ac}|^2$.

There is no free-energy difference between the sequence *AcBaCb*... and the symmetric twin structure *AbCaBc*..., so in experiments we expect a superposition of the scattering from both crystals. The scattering from the sequence *AbCaBc*... may be calculated using the methods of the preceding paragraph. The unit cell of the NaCl twin contains a large sphere at A and a small sphere on the b-interstitial site so the cell form factor, $|F_{Ab}|^2$, is

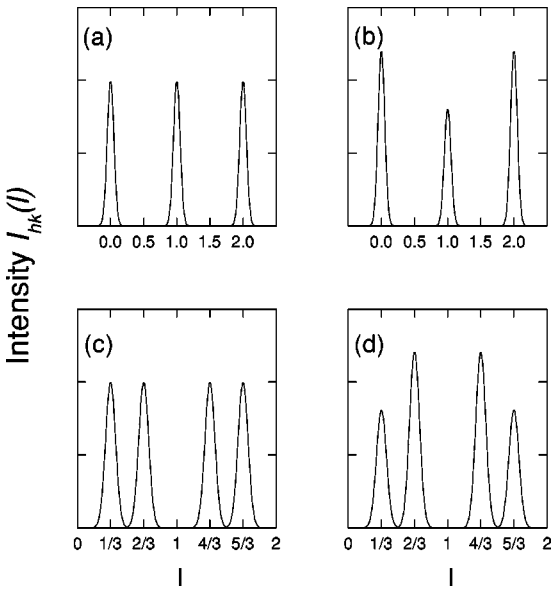

FIG. 9. The intensity distribution $I_{hk}(l)$ along the (h,k) Bragg rods in reciprocal space for a twinned fcc lattice of large spheres [(a) and (c)] and for the twinned NaCl lattice [(b) and (d)]. The top figures [(a) and (b)] show $I_{hk}(l)$ along $(h-k)=3n$ rods while the bottom set [(c) and (d)] shows the corresponding variation along the $(h-k)=3n\pm 1$ rods. The intensity is calculated assuming an amplitude ratio $b_L/b_S=10$.

$$|F_{Ab}|^2 = b_L^2 \cos^2 \pi\left(\frac{h-k}{3}-l\right) - 2b_L b_s \cos 2\pi\left(\frac{h-k}{3}+l/2\right)+b_s^2. \tag{7}$$

The layer correlation function is simply $y_m = e^{2\pi i m(h-k)/3}$. Following Eq. (6), it is easily shown that nodes of intensity $|F_{Ab}|^2$ occur at $l=n\pm 1/3$ along the $(h-k)=3n\mp 1$ rods and for integral l along the $(h-k)=3n$ rods. Consequently, the twinned NaCl crystal (*AcBaCb*..., *AbCaBc*...) has reciprocal-lattice points at integral l along the $(h-k)=3n$ rods and at $l=n\pm 1/3$ along all other rods. The topology of the reciprocal lattice is identical to the lattice of the twinned fcc crystal of large spheres, outlined in Sec. IV A, so the two structures have identically positioned Bragg reflections.

The change in intensity of the Bragg reflections with superlattice formation depends upon the relative magnitude, b_L/b_S, of the scattering from large and small particles. For a homogeneous particle of radius R, the scattering amplitude is given by the standard expression [33]

$$b(qR) = 4\pi R^3 \Delta n\left(\frac{\sin qR - qR\cos qR}{(qR)^3}\right), \tag{8}$$

where Δn is the refractive index mismatch between particle and medium. The intensity of scattering depends very strongly upon the particle size and so in a binary mixture the large particles scatter light much more efficiently than small particles. For instance, for a size ratio of $\alpha=0.42$ and a scattering vector $qR_L\sim 3.5$ [matching the (001) reflection of the twinned NaCl crystal], the ratio b_L/b_S is about 10. Figure 9 shows the intensity distribution along the Bragg rods

for the twinned NaCl and for the twinned fcc lattice of large spheres, calculated for this amplitude ratio. It is clear that although there are changes in the scattering distribution, the effects are small. For polycrystalline samples, the differences are likely to be even less noticeable since the results in Fig. 9 have to be averaged over all orientations. In conclusion, it is clear that identifying the NaCl superlattice from powder diffraction demands accurate intensity measurements.

VI. CONFOCAL MICROSCOPY

To determine unequivocally if a superlattice is formed in colloidal mixtures of size ratio $\alpha = 0.39$, we have used direct imaging methods. Fluorescence confocal scanning laser microscopy (CSLM) has several distinctive features which make it excellently suited to this problem. First, the use of both a point source and a point detector results in a powerful depth discrimination so only a thin slice of the sample around the focal region of the microscope objective is imaged. Second, the optical resolution is comparable to colloidal dimensions, so single-particle positions can be readily identified. Third, contrast relies on a fluorescent dye, so by labeling alternately the large and small particles in a binary suspension, the structure of mixed crystals may be determined and, finally, suspensions may be studied which are thick enough to show the same phase behavior as they would in the bulk.

High-contrast single-particle images were achieved by incorporating the fluorescently tagged monomer 2-(methyl-(8-nitro-benzo [1,2,5] oxadiazol-1-yl)-amino)methyl methacrylate (NBD-MMA) into the core of the colloidal particle [25]. To clearly differentiate between a NaCl-type superlattice and a crystal of large spheres, only the small particles in the mixture were fluorescently labeled. The large particles are nonfluorescent and are consequently not imaged.

Figure 8(b) shows a fluorescent confocal image of the crystalline phase formed in a mixture of small NBD-labeled and large unlabeled PMMA particles, dispersed in an index-matched mixture of decalin and CS_2, with composition $n_S/n_L = 1$ ($\phi_S/\phi_L = 0.06$) and volume fraction $\phi = 0.532$. The image was recorded about 15 μm below the top glass wall and four days after mixing. Although the image is noisy, it is apparent that the small fluorescent particles are highly localized within a three-dimensional periodic structure. A careful analysis of this micrograph demonstrates that the crystal consists of hexagonal layers of small spheres. The center-to-center distance in the hexagonal plane is 1080 ± 100 nm, which is considerably larger than the diameter ($2R_S = 350$ nm) of the small particles but comparable to the size of the large particle ($2R_L = 896$ nm). This suggests that in the images of Fig. 8(b), the small spheres are separated by nonfluorescent (and thus not visible) larger particles. Given these observations, the view in Fig. 8(b) can be identified as the (001) plane of the *LS* superlattice, in the reduced hexagonal basis (*a*,*b*,*c*) introduced in Sec. V. The crystal is orientated with the close-packed (001) plane parallel to the walls of the cuvette.

A sketch of this close-packed plane is reproduced in Fig. 8(a), from which it is apparent that the center-to-center separation of the small spheres is identical to that of the large particles and equal to the lattice parameter *a*. Further confirmation for this identification comes from scattering measurements. If a *LS* structure is formed, then the intense first Bragg peak at $q_{001} = 7.91 \times 10^{-3}$ nm^{-1} corresponds to a reflection from the (001) planes of the superlattice. The interplane spacing is $c = 2\pi/q_{001} = 794$ nm. The hexagonal (001) planes are close-packed in the *LS* structure so the center-to-center separation within the plane is $a = c\sqrt{3/2}$ or 973 nm. This value is in good agreement with the directly measured interparticle spacing, obtained from Fig. 8(b), of $a = 1080 \pm 100$ nm.

These results demonstrate that a hexagonal layer of large and small spheres, the basic element common to all of the *LS* structures, is formed in a binary hard-sphere mixture of $\alpha = 0.39$. In order to distinguish between NaCl, NiAs, or a random-stacked crystal, it is necessary to determine the stacking sequence of the hexagonal layers. To this end, we recorded a series of confocal micrographs of the same lateral position in the crystal at depths 0.6 μm apart. Unfortunately, thermal drift prevented us from accurately superimposing the optical sections at different heights through the crystal, so we could not reliably identify the sequence of small-particle positions in the stacked layers. Consequently, we are unable to distinguish between NaCl, NiAs, or a random-stacked crystal.

VII. COMPARISON WITH THEORY

A. Size ratio $\alpha = 0.72$

The phase behavior reported above provides broad confirmation of the theory outlined in Sec. II. First, CsCl is not observed in our experiments, in agreement with the predictions of Eldridge *et al.* [14] and Cottin and Monson [5]. This is the case even though the experimental size ratio is close to the peak in the maximum packing curve at $\alpha = 0.732$, where we expect the formation of CsCl, if it is to occur, to be most favorable. Second, with no superlattice we expect the two different-sized spheres to be totally immiscible in the solid state [16] and the fluid-solid phase diagram to contain a eutectic. The equilibrium phase behavior predicted by the immiscible model of Bartlett [34] for a size ratio of $\alpha = 0.72$ is plotted in Fig. 10 together with the experimental samples studied in this work. We find very close agreement between the predictions of theory and observations in samples with either an excess of large or small spheres. So for mixture compositions $n_S/n_L = 0.5$ and 1.0 ($\phi_S/\phi_L = 0.2$ and 0.4) we predict and find crystals of large spheres coexisting with a fluid (the filled circles in Fig. 10) while for mixtures with $n_S/n_L = 13.0$ or equivalently $\phi_S/\phi_L = 5$ (the open circles in Fig. 10) we observe and predict two-phase coexistence between a crystal of small spheres and a fluid. In particular, in the region of two-phase coexistence, we find essentially quantitative agreement with the theory of Ref. [34]. The inset diagram in Fig. 10 compares the large-sphere crystal density predicted (ϕ_{calc}) with values measured from crystallography (ϕ_{exp}) for samples in the fluid-crystal *L* region. As is clear, the theoretical and experimental values for the crystal density are in excellent agreement (the dashed line depicts the condition $\phi_{\mathrm{exp}} = \phi_{\mathrm{calc}}$). Although the phase behavior predicted in Ref. [34] for mixtures rich in small or large spheres is confirmed in this work, there is clearly a striking disagreement in samples with a significant concentration of both

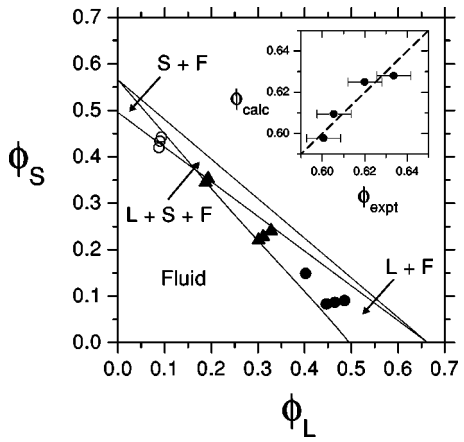

FIG. 10. A comparison between the phases observed and those predicted from the immiscible mixture model [34] for a size ratio of $\alpha=0.72$. See Fig. 2 for symbol definitions. In the inset plot the crystal volume fractions measured (ϕ_{exp}) for mixtures in the two-phase $L+F$ region are compared with predictions from theory (ϕ_{calc}). The line shows the limit $\phi_{calc}=\phi_{expt}$.

large and small spheres (the filled triangles in Fig. 10). Experimentally, we observe amorphous ''glassy'' phases where theory predicts two-phase coexistence.

B. Size ratio $\alpha=0.52$

The observed behavior at this size ratio is broadly in line with simulation predictions. Cell-model calculations [5,35] show that the LS_{13} lattice is stable for size ratios $0.54\leqslant\alpha<0.62$ while the LS_2 lattice is stable over the wider range of $0.42<\alpha<0.6$. The mixtures studied at $\alpha=0.52$. are accordingly just below the lower stability boundary of the LS_{13} structure. Figure 11 depicts the equilibrium phase diagrams (calculated from the cell model) for size ratios $\alpha=0.52$ and 0.54, just below and above this boundary. At $\alpha=0.54$, the region where the LS_{13} phase is formed has already shifted to high densities. With a further reduction in α, the LS_{13} phase disappears completely from the equilibrium phase diagram and is replaced by a wide region of fluid-LS_2 coexistence.

Although the overall pattern predicted by theory is confirmed, there is clearly disagreement in matters of detail. A closer comparison between the behavior of samples with α

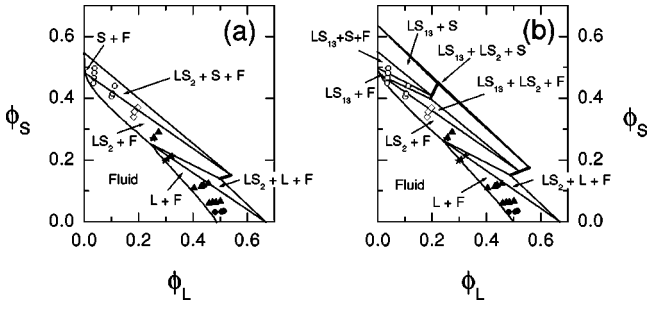

FIG. 11. A comparison of the phases observed in a colloidal mixture of $\alpha=0.52$ with predictions from the cell model for (a) $\alpha=0.52$ and (b) 0.54. The two superlattice phases, LS_2 and LS_{13}, are shown in bold. The symbols denote the experimental data and are defined following Fig. 2.

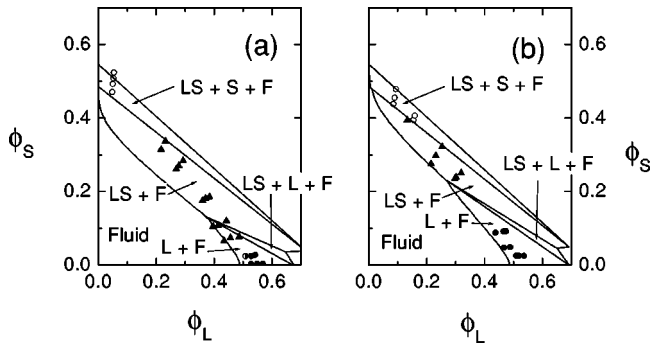

FIG. 12. A comparison between the phases observed and those predicted from the cell model for (a) $\alpha=0.39$ and (b) 0.42. The symbols are defined following Fig. 2.

$=0.52\pm0.01$ (shown by the points in Fig. 11) and the theoretical predictions [35] at $\alpha=0.52$ [Fig. 11(a)] reveals discrepancies. First, and most obvious, LS_{13} is predicted not to be stable. The thermodynamic state predicted for the experimental samples with $n_S/n_L=14$ (the open diamonds in Fig. 11 at $\phi_S/\phi_L=2$) is instead a two-phase (or for the most concentrated sample a three-phase) coexistence between LS_2 and fluid. A thermodynamically stable LS_{13} phase is only achieved if the radius ratio is increased to 0.54 [Fig. 11(b)], above the experimental limit of $\alpha=0.52\pm0.01$. However, comparing the experimental data with the 0.54 predictions, it is clear from Fig. 11(b) that only the most concentrated of the three experimental samples with $n_S/n_L=14$ lies in a region where the LS_{13} crystal is predicted to be thermodynamically stable. We interpret this observation as evidence for kinetics factors favoring the formation of metastable LS_{13} in our experiments. Second, the two most concentrated samples at $n_S/n_L=8$ ($\phi_S/\phi_L=1.1$) which remain amorphous in our experiments (depicted by the central line of solid triangles in Fig. 11) are predicted to lie in a broad zone of two-phase AB_2-fluid coexistence. Third, the samples at $n_S/n_L=2$ and 1 ($\phi_S/\phi_L=0.3$ and 0.15) remain amorphous in our experiments (the filled triangles at the bottom of Fig. 11), whereas we expect formation of a (dense) L crystal and fluid. Although we have concentrated on the discrepancies, on a qualitative level there is a broad degree of agreement between the experimental observations and theory. For instance, the theoretical calculations rationalize why the LS_2 superlattice is not readily formed in samples with composition $n_S/n_L=2(\phi_S/\phi_L=0.3)$, whereas LS_{13} is readily formed in samples of composition $n_S/n_L=13$ ($\phi_S/\phi_L=1.8$). From Fig. 11(a), it is clear that at $n_S/n_L=2$ there is a wide zone of L crystal-fluid coexistence prior to LS_2 formation at higher densities.

C. Size ratios $\alpha=0.42$ and 0.39

There are substantial differences between theory and experiment at $\alpha\sim0.4$ in contrast with the reasonable agreement found at other size ratios. The predictions of the cell theory [35] are reproduced in Fig. 12 for size ratios $\alpha=0.39$ and 0.42, respectively. These diameter ratios are close to the substantial maximum ($\phi_{max}=0.79$ at $\alpha=\sqrt{2}-1$) seen in the close-packing curve for the NaCl structure (see Fig. 1). Consequently, the phase diagrams are dominated by the appear-

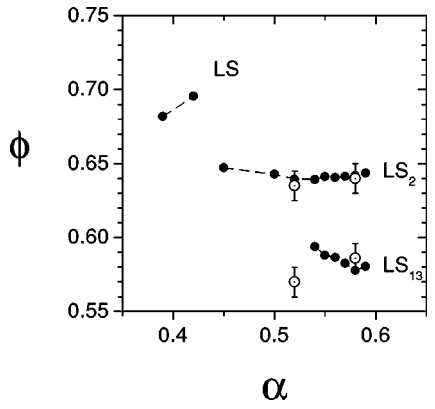

FIG. 13. The lowest densities (ϕ) for each superlattice in coexistence with a fluid, as a function of size ratio α. The filled circles are the simulation predictions of Eldridge *et al.* [14,4] while the experimental values are shown by the open points.

ance of an *LS* superlattice (the LS_2 and LS_{13} phases are no longer stable at these low diameter ratios). A notable feature of the phase diagrams is the very broad region of two-phase coexistence found between *LS* and fluid. The regions of coexistence between fluid and the large or small fractionated crystals, found near each of the axes, are considerably reduced in comparison with the larger diameter ratios (compare, for instance, Figs. 10 and 12). Indeed, comparing the two phase diagrams in Fig. 12, it is clear that the extent of the two-phase *LS*/fluid region expands rapidly with reducing α.

The observed phase behavior is shown by the points in Fig. 12. The disagreements between theory and experiments are most evident in the region where coexistence is predicted between a large-sphere crystal and fluid. The $\alpha=0.39$ mixture studied with confocal microscopy [marked by the half-filled circle in Fig. 12(a)] lies in the middle of this region, yet the data, reported above, clearly identify coexistence between an *LS* superlattice and fluid. A remarkable feature of the remaining data is the strong coincidence between the changes in the observed behavior and the theoretical boundaries, even though the actual phase behavior observed is different from that predicted. So, for instance, all of the mixtures (the filled triangles) which are predicted to lie in the region of two-phase coexistence *LS*/fluid remain amorphous in our experiments, while all those samples (the open circles in Fig. 12) which lie within the three-phase coexistence region between crystals of *LS*, *S*, and fluid separate into a crystal of small spheres and a second fluid phase. At present, the exact reasons for the disparities seen between theory and experiment at small diameter ratios are far from clear. An important factor in the difficulty seen in our experiments in crystallizing the *LS* lattice is probably the high densities predicted for the stable *LS* compound. Figure 13 summarizes the densities, predicted from simulation [4,14], at which each stable superlattice structure is first thermodynamically stable as a function of the relative radius ratio together with the densities found in experiment for the LS_2 and LS_{13} phases (the open circles). Two features are evident from this comparison. First, there is a close correspondence between theory and experiment for the densities found for the LS_2 and LS_{13} phases, and second, the densities predicted decrease quite markedly in the sequence $\phi(LS)>\phi(LS_2)>\phi(LS_{13})$. This order mirrors the observed difficulty with which each superlattice is nucleated. So, for instance, at $\alpha=0.58$, LS_{13} forms within a few weeks while the LS_2 lattice takes several months to grow and the *LS* structure is sufficiently slow as not to be observable at many compositions over the year-long course of our experiments at $\alpha\sim0.4$. It is probable that the difficulty nucleating the *LS* crystal reflects the density dependence of the solid-fluid interfacial tension γ. Little is known about how γ depends on the density mismatch between between fluid and crystal, but it seems clear that the strain at this interface will become larger as the difference in densities between the two phases increases. The large density mismatch predicted for the fluid-*LS* system increases γ for the solid-fluid interface and reduces the rate of nucleation markedly.

VIII. CONCLUSIONS

In this paper we have presented a detailed comparison between the phase behavior and structures found in binary mixtures of colloidal hard spheres and Monte Carlo and cell-model predictions for a mixture of hard spheres. Phase diagrams have been experimentally determined for systems with size ratios of $\alpha=0.72$, 0.52, 0.42, and 0.39 which agree reasonably well with the theoretical predictions. We have observed three distinct types of fluid-solid organization depending on the size ratio α. First, at $\alpha=0.72$ the large and small particles are almost completely immiscible in the solid phase, and the crystalline phase formed at high densities consists of a crystal of predominately either large or small spheres depending on the initial mixture composition; second, reducing the size ratio to $\alpha=0.52$ generates two ordered binary structures which we identify as the LS_2 and LS_{13} superlattice; and finally, at smaller size ratios $\alpha\sim0.4$, we observe an ordered binary *LS* structure which is isostructural with either NaCl or NiAs.

A detailed comparison of our observations with theoretical predictions shows several discrepancies which we attribute to kinetic factors. First, at $\alpha=0.52$ we observe both LS_2 and LS_{13} structures while only LS_2 is expected from cell-model calculations or simulations. The tendency for LS_{13} to be formed at size ratios where it is not stable may reflect the high degree of local icosahedral order present in dense fluids [3]. Second, at $\alpha=0.42$ the observed phase diagram contains a very substantial region of amorphous ordering. The extent of the amorphous region increases as α is reduced to 0.39 and probably reflects the difficulty in nucleating a high-density crystal from a low-density fluid at these size ratios.

ACKNOWLEDGMENTS

This work was supported by the Engineering and Physical Sciences Research Council. We thank Alfons van Blaaderen for his generous assistance with the confocal microscopy experiments. We also acknowledge many valuable discussions with Peter Pusey, Harmut Lowen, and Stuart Henderson.

[1] P. M. Chaikin and T. C. Lubensky, *Principles of Condensed Matter Physics*, 1st ed. (Cambridge University Press, Cambridge, 1995).
[2] P. Bartlett, R. H. Ottewill, and P. N. Pusey, Phys. Rev. Lett. **68**, 3801 (1992).
[3] M. D. Eldridge, P. A. Madden, and D. Frenkel, Nature (London) **365**, 35 (1993).
[4] E. Trizac, M. D. Eldridge, and P. A. Madden, Mol. Phys. **90**, 675 (1997).
[5] X. Cottin and P. A. Monson, J. Chem. Phys. **102**, 3354 (1995).
[6] P. N. Pusey and W. van Megen, Nature (London) **320**, 340 (1986).
[7] S. Hachisu and S. Yoshimura, in *Physics of Complex and Supermolecular Fluids*, edited by S. A. Safran and N. A. Clark (Wiley, New York, 1987), pp. 221-240.
[8] C. J. Kiely, J. Fink, M. Brust, D. Bethell, and D. J. Schiffrin, Nature (London) **396**, 444 (1998).
[9] J. V. Sanders, Philos. Mag. A **42**, 705 (1980).
[10] M. J. Murray and J. V. Sanders, Philos. Mag. A **42**, 721 (1980).
[11] E. Yablonovitch, Phys. Rev. Lett. **58**, 2059 (1987).
[12] S. John, Phys. Rev. Lett. **58**, 2486 (1987).
[13] D. Frenkel, Phys. World **6**, 24 (1993).
[14] M. D. Eldridge, P. A. Madden, P. N. Pusey, and P. Bartlett, Mol. Phys. **84**, 395 (1995).
[15] H. Xu and M. Baus, J. Phys.: Condens. Matter **4**, 663 (1992).
[16] W. G. T. Kranendonk and D. Frenkel, Mol. Phys. **72**, 679 (1991).
[17] S. M. Underwood, W. van Megen, and P. N. Pusey, Physica A **221**, 438 (1995).
[18] A. R. Denton and N. W. Ashcroft, Phys. Rev. A **42**, 7312 (1990).
[19] S. J. Smithline and A. D. J. Haymet, J. Chem. Phys. **86**, 6486 (1987).
[20] P. Bartlett, R. H. Ottewill, and P. N. Pusey, J. Chem. Phys. **93**, 1299 (1990).
[21] M. D. Eldridge, P. A. Madden, and D. Frenkel, Mol. Phys. **80**, 987 (1993).
[22] M. D. Eldridge and P. A. Madden, Mol. Phys. **79**, 105 (1993).
[23] The NiAs structure was not actually included in either calculation. However, the packing efficiencies of NiAs are identical to NaCl and so in the spirit of the maximum packing principle we expect the free energies of these two structures also to be very similar. In that case, the *LS* compound predicted by both of these approaches at $\alpha \sim 0.4$ probably should have either a NaCl, NiAs, or an equivalent random-stacked structure (see Sec. V).
[24] L. Antl, J. W. Goodwin, R. D. Hill, R. H. Ottewill, S. M. Owens, S. Papworth, and J. A. Waters, Colloids Surface **17**, 67 (1986).
[25] R. Jardine and P. Bartlett (unpublished).
[26] P. N. Pusey and W. van Megen, J. Chem. Phys. **80**, 3513 (1984).
[27] W. G. Hoover and F. H. Ree, J. Chem. Phys. **49**, 3609 (1968).
[28] P. N. Pusey, W. van Megen, P. Bartlett, B. J. Ackerson, J. G. Rarity, and S. M. Underwood, Phys. Rev. Lett. **63**, 2753 (1989).
[29] P. Bartlett, P. N. Pusey, and R. H. Ottewill, Langmuir **7**, 213 (1991).
[30] A. Guinier, *X-Ray Diffraction* (Freeman, London, 1963).
[31] The definition of c^* used here is twice the commonly used hcp reciprocal-lattice spacing. As a result, the index l is half the value of the conventional hcp value.
[32] B. E. Warren, *X-Ray Diffraction* (Addison-Wesley, Reading, MA, 1969).
[33] P. Pusey, in *Liquids, Freezing and Glass Transition*, edited by J. P. Hansen, D. Levesque, and J. Zinn-Justin (North-Holland, Amsterdam, 1981), pp. 763–942.
[34] P. Bartlett, J. Phys. C **2**, 4979 (1990).
[35] J. P. Voisey and P. Bartlett (unpublished).